GEOPHYSICS, VOL. 81, NO. 4 (JULY-AUGUST 2016); P. EN29–EN42, 13 FIGS.
10.1190/GEO2015-0356.1

Surface-wave methods for anomaly detection

J. Tyler Schwenk[1], Steven D. Sloan[2], Julian Ivanov[3], and Richard D. Miller[3]

ABSTRACT

Perimeter-defense operations, geohazard assessment, and engineering characterization require the detection and localization of subsurface anomalies. Seismic waves incident upon these discontinuities generate a scattered wavefield. We have developed various surface-wave techniques, currently being fielded, that have consistently delivered accurate and precise results across a wide range of survey parameters and geographical locations. We use the multichannel analysis of surface waves approach to study the multimode Rayleigh wave, the backscatter analysis of surface waves (BASW) method to detect anomalies, 3D visualization for efficient seismic interpretation, BASW correlation for attribute analysis, and instantaneous-amplitude integration in the complex BASW method. Discrete linear moveout functions and f-k filter designs are optimized for BASW considering the fundamental and higher mode dispersion trends of the Rayleigh wave. Synthetic and field data were used to demonstrate multimode BASW and mode separation, which accentuated individual scatter events, and ultimately increased confidence in points of interest. Simple correlation algorithms between fundamental and higher-mode BASW data offer attribute analysis that limits the subjective interpretation of BASW images. Domain sorting and Hilbert transforms allow for 3D visualization and rapid interpretation of an anomaly's wavefield phenomena within an amplitude cube. Furthermore, instantaneous-amplitude analysis can be incorporated into a more robust complex BASW method that forgives velocity-estimation inaccuracies, while requiring less rigorous preprocessing. Our investigations have suggested that a multifaceted surface-wave analysis provides a valuable tool for today's geophysicists to fulfill anomaly-detection survey requirements.

INTRODUCTION

Subsurface anomalies encompass a wide spectrum of geophysical applications including karst dissolution phenomena (e.g., anthropogenic mining and drilling voids, geomorphological void formation); stability assessment of dams, levees, and earth-retaining structures; construction projects (e.g., foundation, structural supports, earthquake hazard, etc.); and perimeter-defense operations (e.g., crossborder and drug tunneling). Dissolution cavities are found across the globe and may form naturally or be accelerated through human activity or inaction. Voids or weak-strength zones are of concern for infrastructure stability and affect all engineering problems. Tunneling activity is a historic and continually developing concern in the United States and abroad. One thing is certain; there is an understood need for geophysical anomaly-detection research and development. Although relevant to many subjects, this research focuses on tunnel discovery.

Tunnel warfare has a long history that stretches centuries before the more recent and well-known activities of both world wars. In recent decades, border stability and related counterterrorism operations have become an integral part of the United States' defense strategy. In 2011, the war in Afghanistan shifted awareness to tunneling activity after a prison break saw nearly 500 inmates escape the Sarposa Prison near Kandahar (Shah and Rubin, 2011). In the United States, ongoing drug tunneling activity along the United

First presented at the SEG 85th Annual International Meeting. Manuscript received by the Editor 1 July 2015; revised manuscript received 27 January 2016; published online 6 June 2016.
[1]Formerly XRI Geophysics, Vicksburg, Mississippi, USA; presently Primal Innovation, Lake Mary, Florida, USA. E-mail: tyler.schwenk@primalinnovation.com.
[2]Formerly XRI Geophysics, Vicksburg, Mississippi, USA; presently United States Army Engineer Research & Development Center, Vicksburg, Mississippi, USA. E-mail: steven.d.sloan@usace.army.mil.
[3]Kansas Geological Survey, Lawrence, Kansas, USA. E-mail: jivanov@kgs.ku.edu; rmiller@kgs.ku.edu.

States-Mexico border brings these issues to the front doors of millions of Americans (Dillon and Lovett, 2013; Santos, 2014). Developing methods to locate and deter tunneling is a social and governmental concern.

Integrated geophysical investigations have been proposed to unearth these tunneling operations. Peterie and Miller (2015) expand previous work with the development of oblique and mode-converted diffraction-processing schemes to locate tunnels. Belfer et al. (1998) use refraction tomography and diffraction stacks to delineate scattering anomalies. Park et al. (1998) incorporate a frequency-variant linear moveout correction (FV-LMO) and Fourier analysis to detect a steam tunnel using diffracted, "backscattered" Rayleigh waves with the theoretical development of the classic backscatter analysis of surface waves (BASW) method. Further research by Sloan et al. (2015) verifies that body-wave diffractions and backscattered surface waves are capable of discovering tunnels across multiple field sites without prior knowledge of their location.

Similarly, geotechnical applications may address a related class of problems with geohazard assessment. Cardarelli et al. (2010) jointly compare electrical resistivity tomography with refraction tomography results to locate a cavity in Rome, Italy. James and Ferreira (2013) discuss the complex nature of discerning anthropogenic cavities with modeled signatures of ground penetrating radar, gravity, and magnetic anomalies. Ivanov et al. (2013) image an anomalous S-wave velocity V_S signature using surface waves over an abandoned salt-injection well field using trains as a seismic source. Samyn et al. (2013) apply crosscorrelation, in a FV-LMO-like operation, and coda-wave interferometry theory to map near-surface anomalies as perturbations in V_S, while concurrently developing an inversion-free 2D V_S map. Finally, Bergamo and Socco (2014) use local energy decay to detect subvertical fault planes of a few tens of meters.

Because surface waves attenuate more slowly than body waves, and often produce stronger relative signatures with standard survey techniques, they are ideal for anomaly detection. Surface-wave methods (SWMs) (Socco et al., 2010), specifically, the multichannel analysis of surface waves (MASW) survey technique (Miller et al., 1999), invert dispersion curves to map V_S as a function of depth (Xia et al., 1999; Anderson et al., 2007; Watabe and Sassa, 2008; Bergamo et al., 2012). MASW V_S sections may be analyzed for low-velocity, low-shear strength anomalies, often in conjunction with a high-velocity halo, which are indicative of voids (Davies, 1951). However, MASW's 1D-V_S inversion scheme is often criticized for its poor lateral resolution. The inherent multichannel sampling of MASW smears the velocity field across the recorded spread. This results in an average path velocity at best (Boiero and Socco, 2011). One research area focuses on resolving the location of lateral discontinuities to better constrain 1D-V_S models or their pseudo-2D interpolation (Hayashi and Suzuki, 2004; Vignoli and Cassiani, 2009). Others implement laterally constrained inversion schemes to enhance 2D structural imaging (Socco et al., 2009).

The forward-propagating energy of a surface wave, moving away from the source across the geophone spread from near to far offsets, may encounter local heterogeneity that causes the wavefield to scatter (Herman et al., 2000; Ernst et al., 2002; Strobbia et al., 2014; Halliday et al., 2015). Our techniques seek to enhance, or image, small-scale scattering phenomena that are inherently below other methods' resolution limits (i.e., refraction tomography, MASW, etc.). We use the "classic BASW" approach to investigate void-like discontinuities in the subsurface by enhancing scattered energy propagating "back" toward the source (Park et al., 1998). Furthermore, we implement a novel processing routine using simple linear correlation of multimode velocity-corrected BASW-image samples. Fundamental and higher mode (HM) dispersion trends formulate separate FV-LMOs that are shown to discretely locate a near-surface, air-filled void in synthetic data. Station- and time-equivalent trace samples are then linearly correlated across the multimode BASW images. Taking this one step further, we separately correlate the band-limited amplitude spectra, and their directional derivatives, of the multimode BASW images. Our correlation treatment reduces the ambiguity of BASW image signatures, particularly, in the presence of coherent noise, by integrating multimode corrections and attribute analysis into a guided interpretation of the classic BASW technique.

Correlation studies led to additional diversification and mode-separation refinement of the BASW method. Hilbert transforms, sorting, and 3D gridding routines are applied to rapidly infer variations in seismic-wave propagation across a site within an instantaneous-amplitude cube. Bow-slice f-k muting and FV-LMOs reveal that scattering may be a dynamic multimode phenomenon that can be imaged discretely by enhancing mode-specific signatures and muting others (Park et al., 2002). To finish, the new complex BASW method incorporates instantaneous amplitude into a more robust and simplistic anomaly imager with limited sensitivity to velocity-correction accuracy and removal of f-k filtering from preliminary processing routines. Although predicated on imaging backscatters, our work also indicates that the disruption of the forward-propagating surface wave and group-velocity characteristics are an untapped resource when using BASW.

This research documents the evolution and recent developments of the classic BASW method that seek to increase the viable detection of underground anomalies using surface waves. These techniques have been field-tested at multiple sites across the globe under ideal and horrible conditions. Whether involved in perimeter-defense operations or research experiments, our methods are shown to accurately detect anomalies at depths ranging from 3 to 22 m, with cross-sectional areas in the order of 1×1 m, in unconsolidated sediments. Mode separation and multimode BASW imaging, multi-image linear correlation, complex BASW, and 3D amplitude-cube visualization are seen as major contributions of this study with each adapted from the classic BASW imaging technique that was first described nearly two decades ago. Although each method stands on its own as an independent anomaly discriminator, a multimethod approach, including methods not documented here, is followed to assure confident results. We propose a multifaceted SWM investigation to localize subsurface discontinuities in future anomaly detection applications (Figure 1).

METHODS

BASW

The classic BASW method involves several processing steps (Park et al., 1998, 2002; Sloan et al., 2010, 2013, 2015); a visual flow is used to help comprehension using synthetic data (Figure 2). Multiple shots are routinely collected at each source station; data are first sorted to discard records and traces that adversely affect signal-to-noise ratios (S/Ns). Coherent energy is then enhanced by stack-

ing common-source gathers to further increase S/N. As with all geophysical surveys, some level of signal degradation is unavoidable with ambient and cultural noise. The use of surface waves and field-acquisition quality assurance gives us a built-in advantage over diffraction imaging, etc., that start with relatively weaker signals and increased sensitivity to S/N. Figure 2a and 2b is included to relate that backscatter signal is often visible on raw shot gathers as distortions in the forward-propagating wavefield and may offer a first-line interpretation of anomalous changes across a site. The f-k filtering then attempts to remove the forward-propagating surface wave to enhance backscattered energy (Figure 2c). Some level of signal distortion is expected with f-k processing. Here, we are most concerned with loss at, and approaching, the apex of backscattered events because we ignore the entire forward-propagating wavefield. This is an intrinsic limit of our processing technique; later sections will discuss how we may implement bow-slice f-k muting to reduce these effects and further enhance BASW imaging.

The velocity function(s), assembled from an MASW study, are then applied to shot gathers through an FV-LMO that flattens the forward-propagating wavetrain and places the locus of backscattered energy along the station axis (Figure 2d). The FV-LMO operation is given by the equation after Park et al. (2002):

$$P_{\mathrm{FV-LMO}}(x,\omega) = \phi_{-}(x,\omega)P(x,\omega), \tag{1}$$

where $P_{\mathrm{FV-LMO}}$ is the phase-shifted 1D Fourier transform, $P(x,\omega)$ of the original time-series data $p(x,t)$, x is the distance from the source, and ω is the angular frequency. The phase shift $\phi_{-}(x,\omega)$ is defined as

$$\phi_{-}(x,\omega) = e^{-ix\omega/C_{\omega}}, \tag{2}$$

where ϕ_{-} implies this as a negative shift to remove intrinsic positive moveout with offset, i is the imaginary unit, and C_{ω} is the phase velocity for frequency ω as defined by the picked dispersion curve.

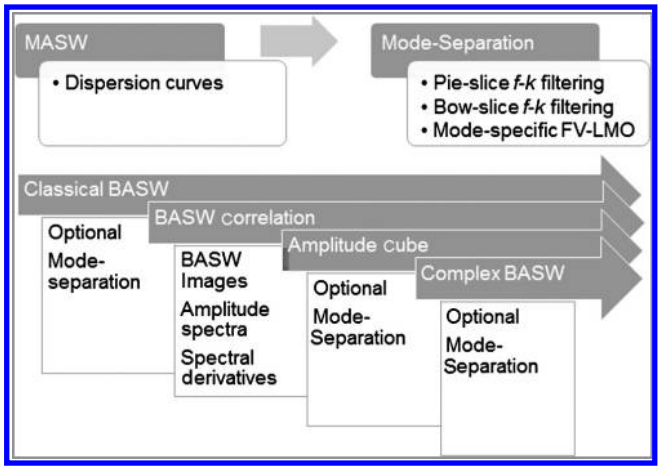

Figure 1. A multimethod assessment increases the odds of finding anomalies through redundancy. The flow chart expresses how MASW is first used to define dispersion curves, which define f-k filters and FV-LMOs that allow for mode separation and enhancement of mode-specific backscatter phenomena. Classic BASW and multimode BASW images may then be used to formulate BASW correlation diagrams. Amplitude-cube visualization and complex BASW take advantage of instantaneous amplitude to image anomalies from a different standpoint.

The phase shift ϕ_{-} is the mechanism that links the BASW velocity correction to the dispersion-curve interpretation of the dispersion image. An inverse 1D Fourier transform of $P_{\mathrm{FV-LMO}}(x,\omega)$ results in a velocity-corrected (phase shifted) shot gather ($P_{\mathrm{FV-LMO}}(x,t)$). The time axis now represents a frequency-dependent transform of the original data. We note that this imaging technique explicitly assumes a linear projection of the scattered surface waves across offset.

Finally, the moved-out gathers are sorted into a common-receiver stack that is referred to as the BASW image. The slope of the back-

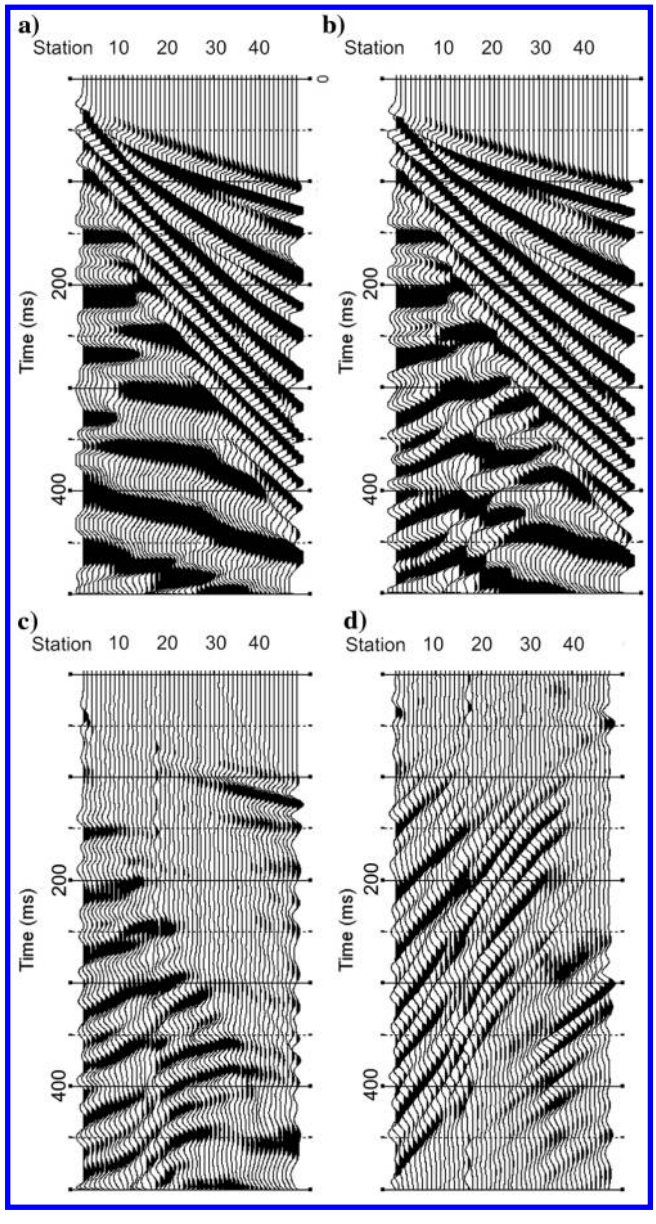

Figure 2. Sequence of processing steps for the BASW method: (a) gather with an undisturbed seismic wavefield generated from a homogeneous layered model, (b) gather with a backscattered signature generated after adding a rectangular void to the model, (c) panel (b) with a f-k pie-slice mute applied, and (d) panel (c) with a FV-LMO applied. The final step is to perform a common-receiver stack to the FV-LMO data. All images use gains to boost the amplitudes of the various signatures.

scattered signature is now opposite that of the original data set. This trend is dependent on the acquisition and display scheme of each survey. Although obvious from the method explanation, the BASW method diverges from diffraction imaging and scattering techniques that seek a total collapse of the scattered wavefield to a localized position.

When velocity varies with depth, surface-wave dispersion results as different frequency components travel within stratified velocity horizons of the subsurface. We use the MASW survey approach and the high-resolution linear Radon transform to analyze Rayleigh-wave dispersion (Luo et al., 2008). As briefly noted in the "Introduction" section, dispersion images are primarily a product of vertical heterogeneity; however, wavefield sampling, transform effects, lateral heterogeneity, and topography can affect dispersion interpretation (Ivanov et al., 2008; Schwenk et al., 2012a). Care must be taken to assess how geometric sampling affects dispersion imaging to assure accuracy of the velocity function(s) across a site. Given those considerations that should accompany any MASW survey, the notion of improper mode identification is less significant as we correct for relatively strong-amplitude trends that represent the average characteristics of a site regardless of mode number.

When velocity structure fluctuates across a site, small perturbations in the velocity field will stack coherently. However, large changes in V_S (> 15%) dictate a change in the correction-velocity function and piecemeal division of the survey line. If multiple velocity corrections are used, the individual results should overlap to aid interpretation across any transition zones. In the presence of complex lateral heterogeneity, each shot gather can be corrected for its own dispersion curve and division of the line becomes unnecessary. Using many 1D velocity corrections may warrant a smoothing regularization of the velocity functions to limit data jitter and interpretation deviations, while enhancing coherency across common-receiver stacks. This is particularly important if automatic max-amplitude picking routines are used during the MASW investigation instead of a smoothly varying curvilinear dispersion interpretation.

Classic BASW focused exclusively on fundamental-mode energy, or followed the apparent curve (Tokimatsu et al., 1992), skipping from one mode to the next without regard for mode separation. The application of multimode velocity corrections necessitates mode separation, if not mode identification. With multimode BASW processing, fundamental and HM dispersion curves produce separate FV-LMOs that discreetly flatten the forward-propagating surface-wave modes.

BASW correlation

Expanding this standard procedure, we correlate fundamental and HM-BASW images to objectify their interpretation. We use the Pearson product-moment correlation algorithm to assess the linear correlation r between both images on a sample-by-sample basis (Pearson, 1895; Dubrule, 2003). That is, we correlate station- and time-consistent amplitude samples across a set number of traces m, a "bin," through the equation

$$r_l = \frac{\sum_{j=1}^{m}\sum_{k=1}^{n}\left(\frac{x_{jk}-\bar{x}}{\sigma_x}\right)\left(\frac{y_{jk}-\bar{y}}{\sigma_y}\right)}{(mn)-1}, \tag{3}$$

where x_{jk} and y_{jk} are the kth samples of the jth trace of the respective BASW images, with n samples in each trace, $\bar{x}$ and $\bar{y}$ are the bin means, and σ_x and σ_y are the bin standard deviations. The defined correlation coefficient, given m and n, is calculated across the entire BASW-image space for each midpoint l. The square of the correlation coefficients r_l^2, collectively r^2 hereafter, are then graphed as a function of the midpoint station of each bin. This coefficient of determination r^2 quantifies the strength of the linear relationship between the data. Increasing the bin size, an expansion of the population size, acts as a quasi-smoothing operation moving away from a local correlation to a relatively more global one. We expect a strong correlation near the axis crossing of the anomaly that declines with offset as the differences between the individual BASW images increase. The selection of bin size is entirely subjective; its purpose is to remove the erratic fluctuations in r^2 that may be found with single trace or progressive bin-width analysis.

We are interested in correlating similar waveforms of the two BASW images. Because we are specifically searching for highly correlated phenomena, data that have an indirect relationship (e.g., $x_{jk} \ll y_{jk}$) or negligible signal (e.g., $x_{jk} \approx y_{jk} \approx 0$) hold no meaningful relation, yet they may drive correlation values at each midpoint calculation. Each bin population set ($A = (x, y)$) may be constrained by a minimum-amplitude threshold defined as

$$B \subset A; B = \{(x,y)|\, x < -z \text{ or } x > z \wedge y < -z \text{ or } y > z\}, \tag{4}$$

where B is a subset of A and z is the threshold value. Eliminating negligible and indirect values accordingly, artificially forces correlation between relatively high-amplitude samples of the data set. This is one regularization scheme of many; review of the crossplots (x versus y) is necessary to curtail outlier influence and correct them appropriately (see Dubrule [2003] for a review of these concepts). As a note of caution, regularization must not skew the intrinsic distribution of the data and contaminate the results.

Correlation of the seismic wavelets evaluates a fundamentally time-variant event (wavelet) with a time-invariant calculation (sample). Attempting to curtail this dichotomy, frequency-domain transforms seek to make a more cohesive comparison of the backscattered energy. Each trace of the BASW image ($g(t)$) is mapped to the frequency domain ($G(f)$) via the 1D discrete Fourier transform, and the amplitude spectra ($A(f)$) is extracted as

$$A(f) = |G(f)| = \sqrt{\{\mathrm{Re}[G(f)]\}^2 + \{\mathrm{Im}[G(f)]\}^2}. \tag{5}$$

Before correlation, the spectra are band-pass filtered to include only those frequencies that are excited by both Rayleigh-wave modes (i.e., the overlapping frequency content of the multimode velocity-correction dispersion curves). The resulting spectra are correlated to infer the frequency dependence associated with the signature of an anomaly.

In addition, the amplitude spectra are filtered with a directional-derivative operator across the station axis $D_{\mathbf{x}}$ to better ascertain lateral transition zones. Considering the case of a single-row grid file with nodes ($Z(x)$) and a node spacing (Δs), the directional derivative is given by the equation after Schwartz (1974):

$$D_{\mathbf{x}}Z(x) = \lim_{\Delta x \to 0}\frac{\Delta Z}{\Delta x} = \frac{dZ}{dx}, \tag{6}$$

which can be approximated across the node (Z_x) by

$$\frac{dZ}{dx} \approx \frac{Z_{x+1} - Z_{x-1}}{2\Delta s}. \quad (7)$$

The correlation of these amplitude-spectra derivatives is the final attribute analysis incorporated into the classic BASW routine.

Amplitude cube and complex BASW

The next method is a mixture of transformations, sorting procedures, and 3D gridding. This research developed during standard quality-assurance investigations of the processing steps of the classic BASW technique. We found that inferring lateral variation in seismic sections was improved when scanning through common-offset and common-receiver sorted gathers. As an additional refinement, we use the Hilbert transform (Taner et al., 1979) to calculate the trace envelope of common-source stacks with no f-k filtering or FV-LMO. The instantaneous-amplitude data are then sorted and gridded into a 3D lattice (i.e., common offset versus common receiver versus time). The lattice-display format allows lateral discontinuities to be more easily localized by scrolling through the various slice planes. We refer to this 3D visualization as the amplitude cube.

The correlation analysis and amplitude-cube findings led to a more extensive investigation into separating the Rayleigh wave into mode-specific units. Processing attempted to isolate fundamental and HM wavefields through surgical f-k muting of the forward-propagating surface waves using bow-slice f-k filtering techniques. This treatment also minimizes the destructive effects of broader pie-slice f-k mutes (e.g., ringing, spectral smearing, and coherent-signal loss). After filtering, multimode FV-LMOs, and their BASW images, convey the dispersive nature of scatters as each velocity correction separately images the void with a discrete signature. Squiggle traces overlay instantaneous-amplitude plots to emphasize dynamic changes in trace bandwidth and amplitude.

Finally, we incorporate the instantaneous-amplitude attribute into a complex BASW processing scheme in a continuation of the amplitude-cube investigations. The complex-trace envelope is computed from raw, unfiltered data traces. Here, no f-k filtering is applied, and we use a constant-velocity LMO that is initially the average V_S to the depth of a suspected anomaly or, more commonly, a range of velocities that are characteristic of the site. In the absence of other geophysical methods to constrain the velocity model of a site, a band-limited average of the fundamental or HM dispersion properties of a site may be sufficient for preliminary investigations. While still referring to a single velocity LMO, subsequent sections may use the term HM velocity correction, etc., with the complex BASW method. This gives the reader a relative sense of the velocity correction in comparison with the other methods. A common-receiver stack completes the routine.

SYNTHETIC DATA RESULTS

We first look at synthetic seismic data to introduce the multimodal BASW concept with the clarity only available through interpreting synthetic signatures. Schwenk et al. (2012b) develop a velocity model representative of a test site located near Yuma, Arizona (Figure 3); we use that model to demonstrate multimode FV-LMO uncertainty effects, associated fluctuations in the correlation diagram given that uncertainty, and geometric sampling effects on BASW imaging. A finite-difference elastic-wave algorithm after Zeng et al. (2011), generated synthetic seismograms using a 35 Hz center-frequency, first-order, Gaussian-derivative source wavelet. A 336 station fixed spread with a 1.2 m geophone spacing was modeled with a 2.4 m source interval. The 1.2×1.5 m air-filled void is 9.1 m deep, and the left corner of the void is at station 1170. Subsets of these data with a 36.6 m source offset (SO) and a rolling 24-phone spread were processed to mimic similarly acquired field data presented later.

Standard pie-slice f-k muting is followed by applying separate fundamental and HM FV-LMOs; review of the BASW images verify both dispersion corrections, properly place the backscattered locus at station 1170 (Figure 4). In comparison with the fundamental (Figure 4a), the HM FV-LMO (Figure 4b) shifts the tails of the signature to higher stations. However, both BASW images display ringing that extends above and below the high-amplitude core of the linear trend and makes interpretation difficult. This radiation pattern will become muddled as S/N fluctuations and attenuation degrade the scattered signal in field settings. Furthermore, natural heterogeneities will superimpose and mask void signatures in real-world settings. The relative difference in frequency content is clearly discerned through visual inspection of the multimode BASW images. Following surface-wave theory, this makes sense as HMs are generally excited along higher frequency bands relative to the fundamental mode.

Assessing the effect of uncertainty in the velocity-correction function, we also correct for a $\pm 15\%$ end-member shift in the dispersion curve (i.e., the error bars in Figure 4h). Some oscillation above and below the central trend is expected during a dispersion picking routine. Erratic velocity variation across small frequency steps violate theoretical principles and should never be included in standard SWM inversion, but are too often interpreted as real rather than erroneous imaging artifacts. End-member corrections that still honor the global curvilinear trend are, although extreme, reasonable deviations to the reference curve. The overall effect of such uncertainty on the BASW images is to radially pivot, or phase shift, the signature wavefield about the station-axis locus to earlier or later time. An undercorrection ($+15\%\ C_\omega$) will result in a smaller phase shift, effectively moving the signature to later time and the locus, in this example, to higher stations (Figure 4c and 4d). An overcorrection ($-15\%\ C_\omega$) will do the opposite, shifting the locus to lower stations and the signature up in time (Figure 4e and 4f). This emphasizes the apparent subjectivity of BASW image interpretation when using FV-LMO that deviate from the true velocity model.

Scattered surface-wave events are a multimode response that incorporates the constructive and destructive interference of mode-

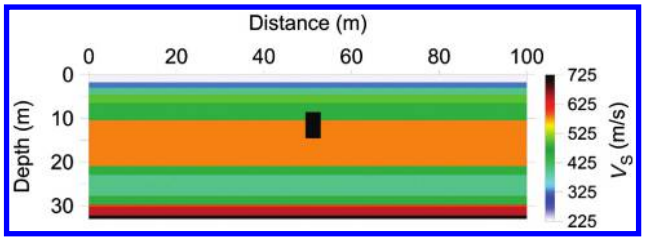

Figure 3. The V_S model for the Yuma site, with exaggerated tunnel not to scale (black rectangle).

specific phenomena prior to, and after, encountering a subsurface anomaly. Correlation analysis takes this multiplicity into consideration by quantitatively measuring the linearity between the multimode BASW images on a sample-by-sample basis. A nine-trace-bin correlation of the synthetic data results in a peak value within one station of the void at station 1171, toward the right edge of the tunnel, versus the incident face at station 1170 (Figure 4g). Applying correlation analysis to the bulk-shifted velocity corrections (i.e., $\pm 15\%\ C_\omega$) results in a change of the overall character of the correlation trends, ultimately deviating the peaks by up to three stations from the reference case (1172 at $+15\%\ C_\omega$ and 1174 at $-15\%\ C_\omega$). The HM deviation to higher stations and the ringy nature of both signatures led to a secondary correlation lobe at higher stations. When necessary, and based on site characteristics, an arbitrary r^2 background-level threshold is set to limit initial points of interest (POIs).

Finally, we assess the geometric sampling effects of various acquisition setups on the BASW images. By varying SO and spread length, we may assess how differential sampling of the surface wavefield affects the final results of BASW imaging. Figure 5 sets up a grid of acquisition parameters that include 2.4, 28.8, and 57.6 m SOs in conjunction with streamer lengths of 24, 48, and 72 geophones. For the 24-geophone spread, a relatively large SO results in a smearing of the signature across the station axis to, in this case, lower stations. This is an effect we attribute to a boost of the HM component of the signature that is overcorrected by the fundamental-mode velocity correction and differentially amplified at far offsets (Figure 5d and 5g). This effect is largely negated by longer spread lengths and their associated increase in fold, which amplify the S/N of the core fundamental signature (Figure 5f and 5i). The numerical modeling ignores attenuation, leading to relatively stronger signatures in relation to real-world data. Attenuation would likely reduce the S/N gains and insensitivity to SO found with longer spread-length acquisition schemes, particularly at farther offsets from the anomaly.

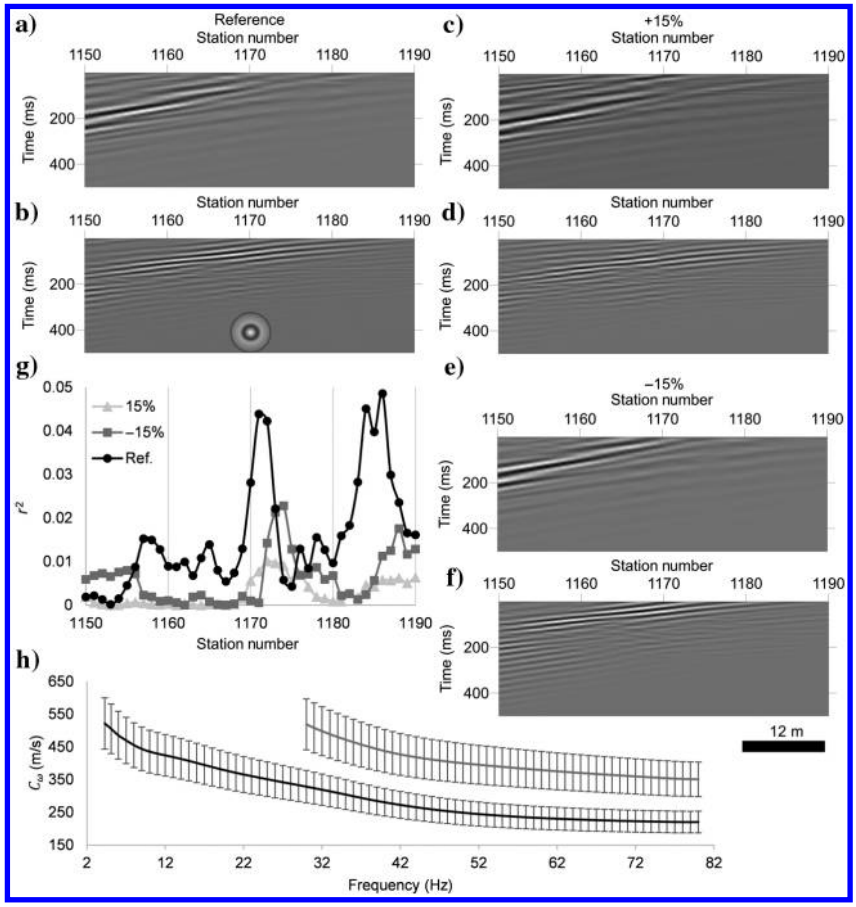

Figure 4. BASW images for the (a, c, e) fundamental and higher mode (b, d, f) FV-LMOs and (g) their correlation results for the Yuma model data. (h) Uncertainty in velocity is expressed as a $\pm 15\%$ change (i.e., the extent of error bars) in the reference fundamental (black line) and higher mode (gray line) curves. These and all future BASW images have been smoothed with a difference of Gaussian filter for display purposes. The tunnel is located at station 1170 (bull's eye). Incorrect correction velocities skew the axis crossing and character of the BASW images leading to lower relative correlation peaks at 1172 ($+15\%\ C_\omega$) and 1174 ($-15\%\ C_\omega$) versus the reference model peak at 1171.

FIELD DATA RESULTS

The authors have acquired and/or processed data from multiple sites along the United States-Mexico border, at test facilities across the globe, and multiple sites in Afghanistan. The following section gives several field examples of the SWMs discussed previously. Most data sets were collected with a land-streamer array, with 24 pods of 4.5 Hz vertical geophones every 1.2 m (4 ft). The source is an accelerated weight drop, which transfers more consistent, high-energy, broadband impacts with dramatically reduced manpower in comparison to the time-honored sledgehammer. Military and law-enforcement operations, among others, benefit from the small footprint, speedy acquisition, and limited personnel requirement of the land-streamer system. Comparisons between fixed spreads and land-streamer data confirm insignificant differences between the qualities of the measured signals (van der Veen et al., 2001). To restrict artifacts caused by low-fold at the end of each line, figures are cropped up to one streamer length from the first and last receiver station; beyond that, the full acquisition line is displayed for each figure.

Correlation analysis

Field data were collected perpendicularly over a man-made tunnel test site near Yuma, Arizona. A vertical shaft and horizontal digging ensured the natural state of the overburden was not disturbed. The tunneling process was similar to that found with clandestine examples along the United States-Mexico border and elsewhere. Two land-streamer lines are presented, running parallel to each other and separated by 10 m laterally. With a unique SO, both surveys were recorded using two-station source rolls in standard off-end acquisition. The site is at the edge of an alluvial basin, with variable sand, clay, and silt content, negligible soil moisture and grade.

In an area with low cultural and ambient noise levels, the first survey was collected with a 36.6 m SO. Even with minimal noise, the BASW image exhibits numerous backscatter signatures not related to the tunnel (Figure 6a). These are thought to be products of geologic anomalies, such as stratigraphic lenses, pinchouts, and larger clasts. The convoluted nature of the image is typical of data sets acquired by the authors across the United States and abroad. Correlation analysis (Figure 6b) allows a guided interpretation that offers four initial POIs. These points align well with strong-amplitude linear trends of the BASW image, including the tunnel signature at station 1058 (Figure 6c). We may speculate that nearby wells contribute scattered energy, although at approximately 10 m away, we hesitate to assign a direct interpretation to these features.

At this stage, other methods would be required to further reduce the POI. Collecting two parallel or overlapping survey lines would constrain the interpretation of the BASW images with or without the use of correlation analysis. Because we are sampling the local structure from one direction, with a singular source-roll movement, we may not adequately characterize the directionality of surface-wave propagation. Later examples will relate the advantages of combining forward- and reverse-acquisition schemes into one BASW routine. To better assess constructive and destructive interference and reduce initial POI, we suggest analyzing dual-incidence data sets individually, before combining them, for greatest comprehension.

To confirm repeatability, another line was collected at the Yuma test site with several months passing between surveys. This survey was acquired with a shorter SO of 29.3 m. The processing was further refined by amplitude thresholding; only relatively strong-amplitude nodes of the multimodal BASW images are correlated (Figure 7a). Here again, the method properly located the tunnel at station 1020. The results suggest the method is repeatable across temporal variations in site condition and mechanical drift, while also being insensitive to changes in acquisition parameterization (i.e., SO changed from Figure 6). By evaluating Figures 6b and

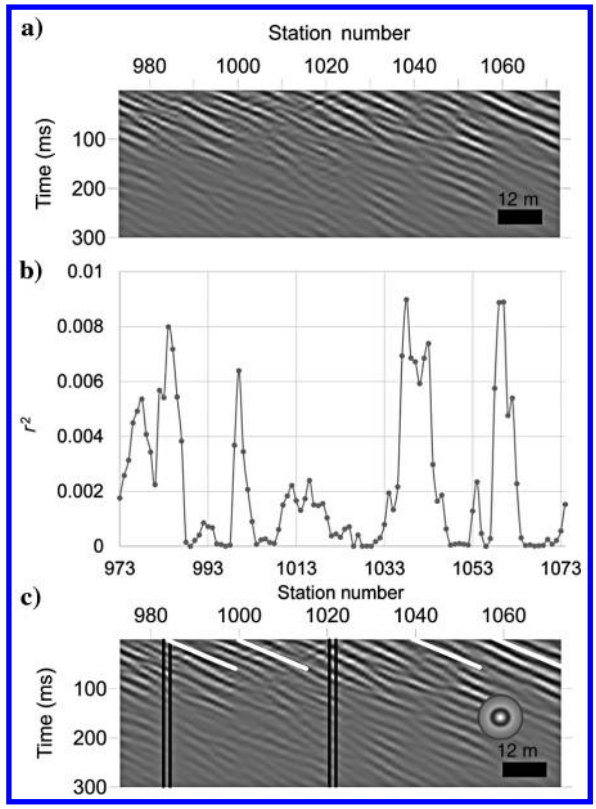

Figure 6. (a) BASW image for the 36.6 m SO Yuma field data with multiple linear signatures. (b) Correlation diagram denoting several POI (peaks) including the tunnel at station 1058. (c) Interpreted BASW image with POI (the slanted white lines that follow linear data trends) and project from the peaks of the correlation diagram (or their midpoints) and the true tunnel location (bull's-eye). The vertical parallel lines represent wells that are offset perpendicularly from the line by approximately 10 m.

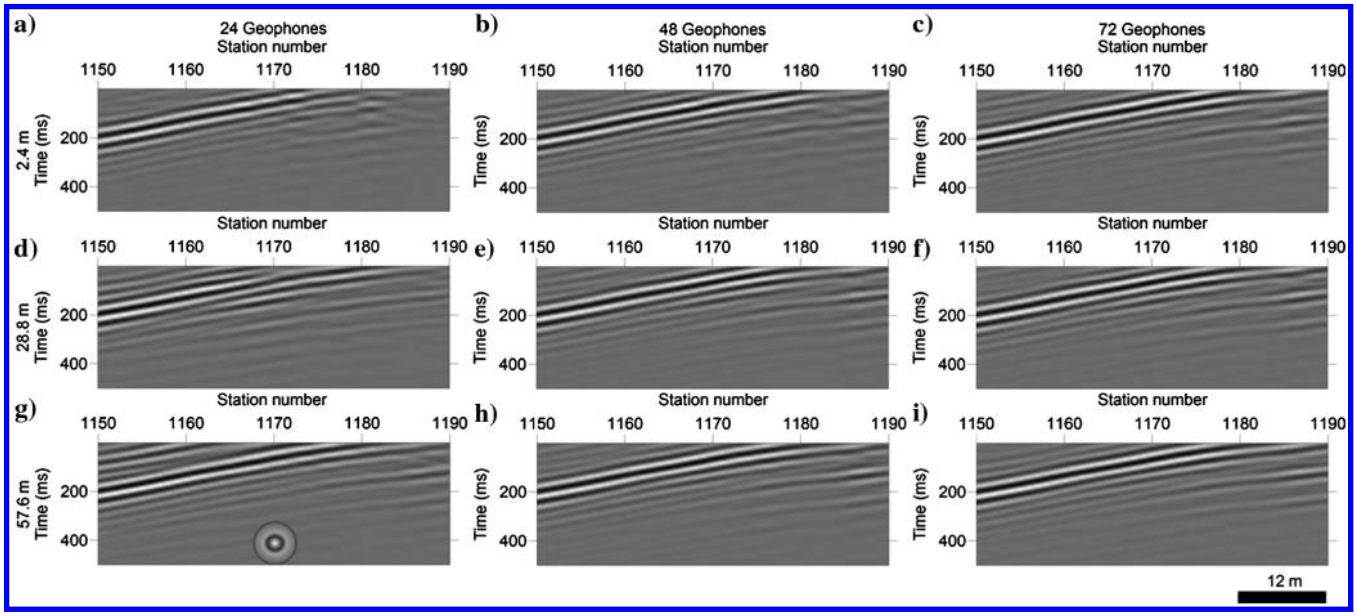

Figure 5 . Geometric sampling effects on BASW images are analyzed by varying spread length and SO within a roll-along acquisition pattern using a fundamental FV-LMO. The various subsets include (a, d, g) 24 geophones, (b, e, h) 48 geophones, and (c, f, i) 72 geophones; (a-c) 2.4 m SO, (d-f) 28.8 m SO, and (g-i) 57.6 m SO. The tunnel is marked by the bull's eye and located at station 1170.

7a, an interpreter would eliminate all POI other than the tunnel location (the station numbers are not consistent).

A final land-streamer data set was recorded with a 24.4 m SO over a clandestine 6.4 m deep tunnel in Afghanistan and analyzed using the amplitude-threshold correlation approach (Figure 7b). The tunnel anomaly is similar to the previous instances with the peak shifted two stations from the known location at station 3995. Like the synthetic data, the correlation diagram exhibits two peaks, whose projections nicely bound the tunnel backscatter. Side lobes seem to occur with some frequency. With clear anomaly boundaries, side-lobe interpretation is straightforward — we interpret the "leading edge" of the backscatter as the anomaly location, and the secondary peak corresponds to the "back end" of the wavetrain and a lateral loss of signature amplitude. Blurred transition zones will make interpretation more difficult. Review of other sites should resolve whether these lobes may be used as significant discriminators or are a random quality of the study group.

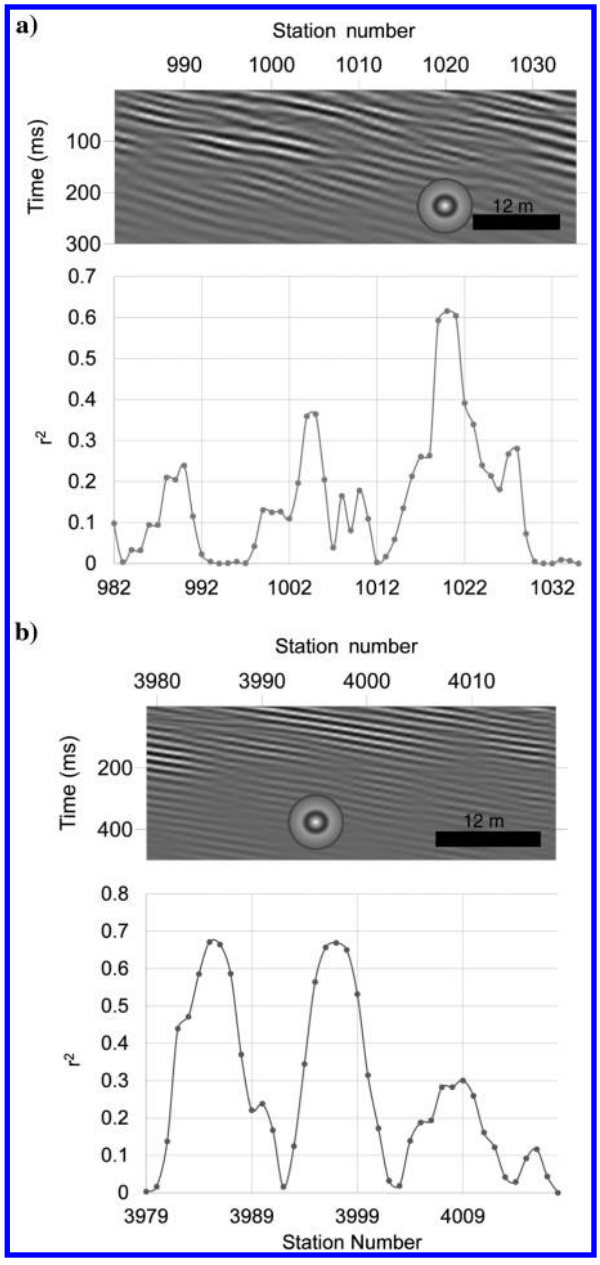

Figure 7. (a) BASW image and the correlation diagram optimized using amplitude thresholding at the Yuma tunnel site set at a different lateral location and collected with a 29.3 m SO (versus Figure 6). (b) BASW image and amplitude-threshold correlation diagram for a clandestine tunnel in Afghanistan. Again, tunnel locations are detailed by the bulls' eyes.

The BASW routine is next augmented with spectral analysis and modal correlation. Returning to the Yuma data at the 36.6 m SO, the BASW amplitude spectra are calculated and then correlated (Figure 8a). The directional derivatives of the amplitude spectra are correlated in the final breakdown (Figure 8b). Transforming to the frequency domain gave a dramatic increase in lateral resolution and a reduction in false positives. The triad of squiggle, spectral, and spectral derivative correlation diagrams (Figures 6 and 8) led to a singular POI corresponding with the tunnel location. This multiplicity provides an integrated interpretation honoring the amplitude, frequency, and dispersive character of the data set. Obtaining these attribute analyses resulted in coincident data sets that independently verified the tunnel location, while eliminating the need for parallel or dual-incident seismic surveying.

Amplitude cube and wavefield separation

Moving to another test site, 3D visualization and multimode BASW highlight wavefield separation. A land-streamer survey crossed perpendicularly over a horizontally dug, 3 m deep tunnel with a 14.6 m SO. The amplitude cube gives a one-sided signature

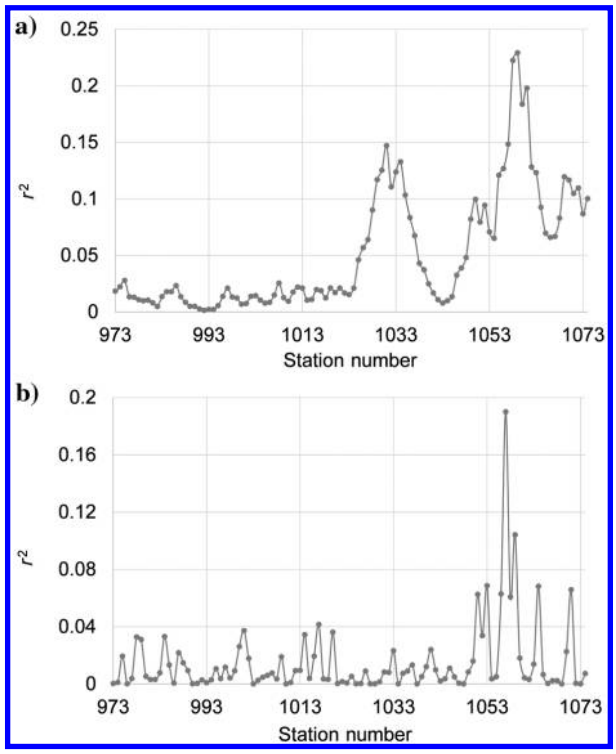

Figure 8. Following from the Yuma data in Figure 6. (a) Correlation diagram of the fundamental and HM amplitude spectra. (b) Correlation diagram of the spectral derivatives. In comparison with the squiggle correlation diagram of Figure 6, frequency-based calculations resulted in a dramatic increase in lateral resolution.

with a low-amplitude zone (Figure 9a) opposing a high-amplitude anomaly (Figure 9b). The anomaly can be traced across common offset with an apparent moveout emanating from the tunnel at station 1018. The lateral variation in velocity structure results in a somewhat haphazard common-offset slice, although this complexity does not overshadow the tunnel signature.

Interestingly, our first revelation was the dominance of the forward-propagating wave within the amplitude cube (Figure 10a). The high-amplitude signature is not a backscatter (receiver-to-source propagation); it is a disruption of the forward-propagating surface wave (source-to-receiver propagation) and is decimated by a forward f-k filter (Figure 10b). Combining forward- and reverse-source rolls increases the coherence and linearity of geologic events, while aiding interpretation with semisymmetrical coincidence of the tunnel signatures (Figure 10c).

Applying this information to the classic BASW technique, we fashioned mode-specific f-k mutes and FV-LMOs to accentuate individual scatter events of the 3 m tunnel with a shorter SO of 7.3 m (Figure 11). The scattered loci of the multimode BASW images are spread across several stations (i.e., 1018−1021). Relatively small adjustments to the correction velocity (<10% C_ω) would correct this; however, the authors wished to show the deviation common with field surveys given a subjective dispersion interpretation. Similar to the 3D visualization results, a dominant portion of the scattered energy resides in the forward-propagating wavefield. This fundamental-mode phenomenon was enhanced with an HM f-k filter and an HM FV-LMO (Figure 11b). Adding a fundamental f-k mute decimates the signal and reinforces our interpretation (Figure 11c). The refractive deflection of the forward-propagating fundamental mode deviates less than 10% C_ω from the phase velocity of the undisturbed wave. It lies within the tapered envelope of the mode-specific fundamental f-k mute. Integrating forward- and reverse-direction rolls illustrates the close relationship between the BASW image and the amplitude-cube scheme (Figure 11d).

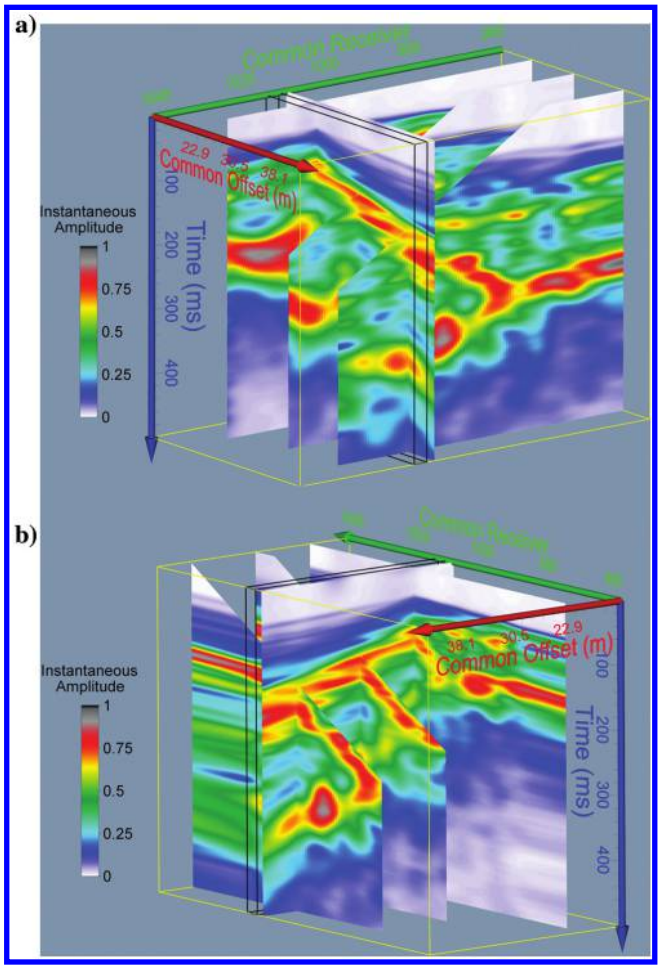

Figure 9. Amplitude cube for a field data set more than a 3 m deep tunnel with a signature that includes (a) a shadow zone opposite (b) a high-amplitude tunnel anomaly. Artifacts are apparent at the edges of the common-offset slices. They are a product of poor receiver coverage and/or fold for the particular offset-receiver pairs.

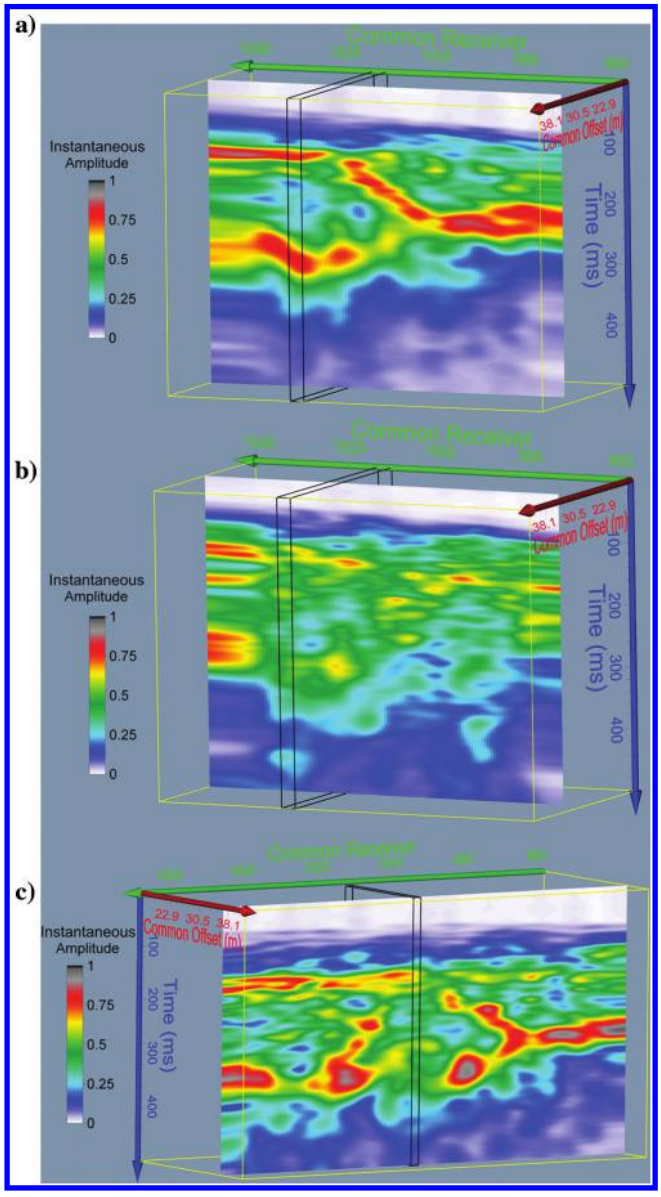

Figure 10. Amplitude cube comparing the (a) full-wavefield and (b) primarily backscattered energy. (c) At a farther-offset slice with integrated forward- and reverse-source rolls, we retrieve a semisymmetrical event emanating from the tunnel location.

Complex BASW

Finally, instantaneous-amplitude analysis is incorporated into the BASW routine. We look at two data sets including a clandestine example and a test site. To demonstrate a range of investigation depth, we review geographically dispersed tunnels as deep as 22 m in unconsolidated sediments. The complex BASW results again use forward- and reverse-acquisition to highlight semisymmetrical signatures.

Starting with the 3 m test site with the 7.3 m SO data, the complex BASW approach depicts a lateral discontinuity at the tunnel location at station 1018 (Figure 12a). The signature manifests as a shift in the seismic horizons of the image. The velocity structure will ultimately dictate the trend, but an inverted "V" is a prominent discriminator that follows the interpretations of the amplitude-cube findings (Figure 10c) and classic BASW imaging (Figure 11d). Our next case is a clandestine tunnel at 22 m deep (Figure 12b). The data set was collected with an 1 m geophone spacing, a one-station source roll, and a fixed 72-channel spread. The complex BASW image is remarkably similar to the previous example. Amplitude trends are comparable across the two results, matching the structural horizons and lateral amplitude deviations.

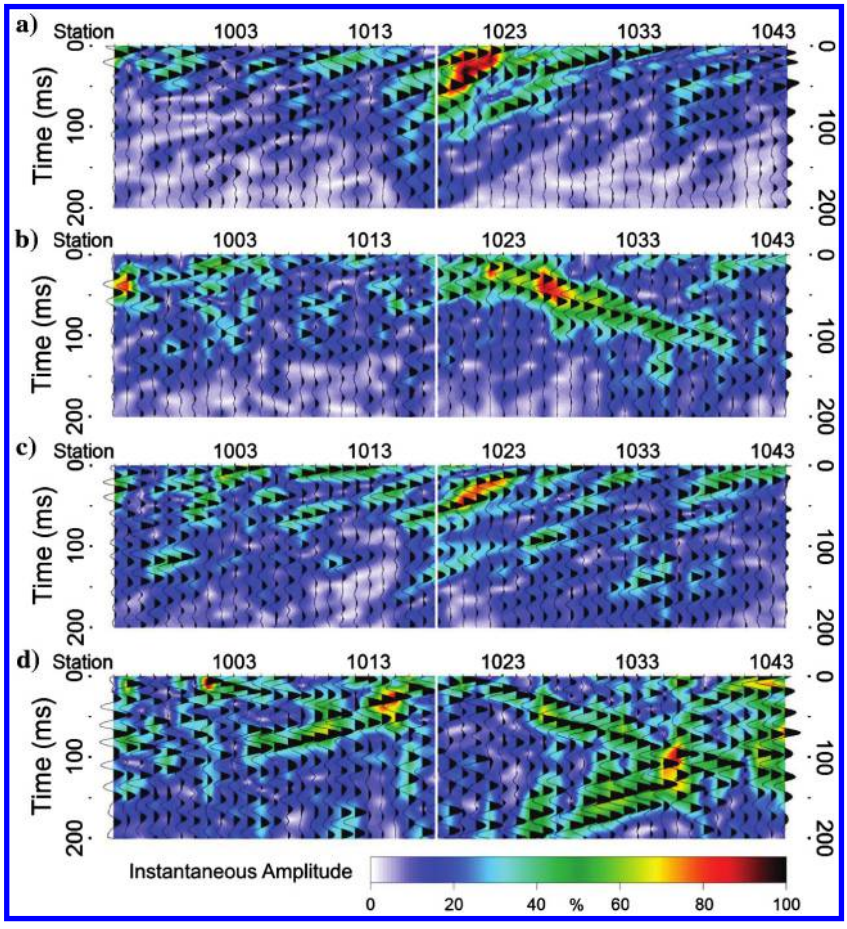

Figure 11. Wavefield separation using mode-specific f-k mutes and variable FV-LMOs with classic BASW. From top to bottom: (a) standard processing using a fundamental f-k mute and a fundamental FV-LMO, (b) HM f-k mute and an HM FV-LMO, (c) fundamental and HM f-k mute(s) with an HM FV-LMO, and (d) a forward and reverse line merged into one routine with an HM f-k mute and an HM FV-LMO. The white vertical line is the approximate tunnel location (station 1018). Seismic squiggle traces overlay instantaneous-amplitude transforms to enhance dynamic changes in amplitude and bandwidth.

DISCUSSION

Although processing was not tuned to enhance tunnel signatures over that of the background, the tunnel locations and depths were known for all the examples given. A detailed analysis of survey notes and raw gathers should always play a role in the evaluation of POI. These are used for classifying known anomalies (false positives) and providing a preliminary interpretive tool for POI. For instance, a booming backscatter signature across multiple shot gathers should be explained; but, a visual signature on shot gathers is not required or expected during an operational survey or to verify another method's results. Similarly, a priori information on an anomaly's general depth or location will not steer processing in one direction or another, initially. Every survey is approached with the same tunnel-detection toolkit, and after an exhaustive parameter optimization, all POI are cataloged. Only then may a priori information be used to guide processing and the production of auxiliary data sets. With classic BASW methods, FV-LMO frequency bands may be used to enhance relatively deeper (lower frequency) or shallower (higher frequency) events following the depth-of-penetration relationship of SWM. Such characterizations will usually elevate known trends through S/N and coherence enhancements that help interpretation. Actually characterizing an anomaly's depth is still subjective and outside the scope of these methods beyond vague and imprecise estimates that are not universally accepted.

This work does not promote a strict comparison of methods across every site. That is intentional and stems from the reality that many methods will fail, sometimes completely, in detecting anomalies at certain locations. POI confidence levels do gain more support given a multimethod agreement, but we cannot always depend on such unambiguous reinforcement. There is no one-size-fits-all solution, and we follow the "all-for-one and one-for-all" mentality in which each method stands alone, but may support the others, increasing the probable detection of anomalies.

Appreciable surface-wave dispersion will result in dissimilar patterns of propagation based on the individual frequency components (wavelengths) of each excited surface-wave mode. Given their discrete velocity-propagation characteristics, each modal wavefield may be described by separate dispersion curves. With proper coupling of the anomaly and the various modes of the dispersive wavetrain, our results verify that the inclusion of a lateral discontinuity in a "dispersive model," or a velocity model that excites appreciable surface-wave dispersion, will generate correspondingly dispersive scatters. This is implied by the discrete imaging of the scatterer using a discrete FV-LMO and a multimode

BASW processing scheme that generates multimode BASW images (Figure 4). This is, of course, a generalization as each site's surface-wave excitation and modal interaction with an anomaly will vary.

The geometric sampling analysis (Figure 5) suggests shorter offsets, or a combination of longer offsets and longer spread lengths, optimizes anomaly interpretation, at least for this site. We speculate that in real-world settings, the S/N loss with increased offsets and superimposed scattering events would likely reduce the apparent benefit of longer spread lengths and their increased fold. We note that both Yuma surveys fall between Figure 5d and 5g, had convoluted anomaly signatures, and still performed well when using the correlation analysis. In comparison with geometric sampling effects, this study suggests the accuracy of the velocity correction plays a stronger role in influencing the axis crossing of anomalies.

The Yuma tunnel was professionally surveyed to a known location of ±1 station. The Afghani tunnel was not surveyed, but was reported as within 1 m of station 3995 (approximately ±1 station). These uncertainties put peak correlation values within ±1 station of the tunnels. BASW correlation reduced the subjectivity of inferring the axis crossing, and added additional attribute analysis to identify higher confidence POI.

With the application of individual FV-LMO velocity corrections, changes in velocity structure across offset will result in relative shifts of the linear projection of scatters. We heavily rely upon the choice of representative curves because they will influence the interpreted location of anomalies. Our uncertainty analysis (Figure 4) reinforces this concept. Where the true velocity correction will place the leading edge of the signature at the tunnel location, errors in the FV-LMO will shift the apparent location of an anomaly to higher or lower stations. A seasoned processor may be able to interpret these fluctuations by analyzing multimode BASW images, but accurate velocity characterization remains essential with correlation analysis and a multimode BASW scheme. Furthermore, it is worth mentioning that the correlation technique may not be applicable to all survey locations. Correlation analysis is contingent upon HM generation, which may be absent or laterally inconsistent in certain environments.

An in-depth synthetic modeling campaign would be needed to assess the resolving power of these techniques in different structural domains and in the presence of anomaly clusters. When multiple anomalies exist laterally, they will superimpose and destructively interfere using SWM techniques. The severity of the interference caused by multiple anomalies will be affected by their size, shape, lateral and vertical separation, geometric sampling, the geologic model and surface-wave excitation, and the relation of the anomalies in reference to a geologic structure. Strong lateral-velocity variation may also provide significant challenges to anomaly detection even with the proposed station-by-station FV-LMO processing scheme.

The amplitude cube allows a quick and efficient solution in interpreting seismic phenomena relative to background structure. The division of the seismic wavetrain into the offset and receiver domains emphasizes variations not easily seen on shot gathers or BASW images alone. The amplitude cube clearly demonstrates that scatterers appear as multiple, time-lagged events separated across offset slices. We image a frequency-dependent phenomenon corresponding to the multimode generation, particle motion, and dispersive coherence (i.e., interference, mode separation in time and phase velocity, etc.) of the forward-propagating wavefield at the anomalous interface. Differential sampling of the surface wave, with relatively near or far offsets, will result in dynamic recordings of irregular responses. However, the 3 m deep tunnel was showcased across two different SOs with no negative consequences.

Interpretations extend from the common-offset and common-receiver domains of the amplitude cube. The common-offset slices are the primary anomaly discriminator due to the relatively smaller distortion apparent on common-receiver slices. Collecting longer offsets allows for more time separation between individual wave phenomena (i.e., direct, refracted, and surface-wave modes), which makes it easier to interpret anomalous signatures on common-offset slices. At some inflection point, near offsets will result in wave superposition and hamper anomaly detection. The common-receiver slices are secondary to anomaly interpretation, but primary for background-wavefield interpretation. The dynamic switching between both domains offers great insight into local wave-propagation characteristics.

As with classic BASW, the wavefield may be manipulated, separated, and imaged in mode-specific units with the complex BASW method. Research suggests that the complex BASW images are more or less shifted in time with increasing linear moveout corrections (Figure 13). This last data set was acquired with a 21.9 m SO using the land streamer with only one pass over the 3 m

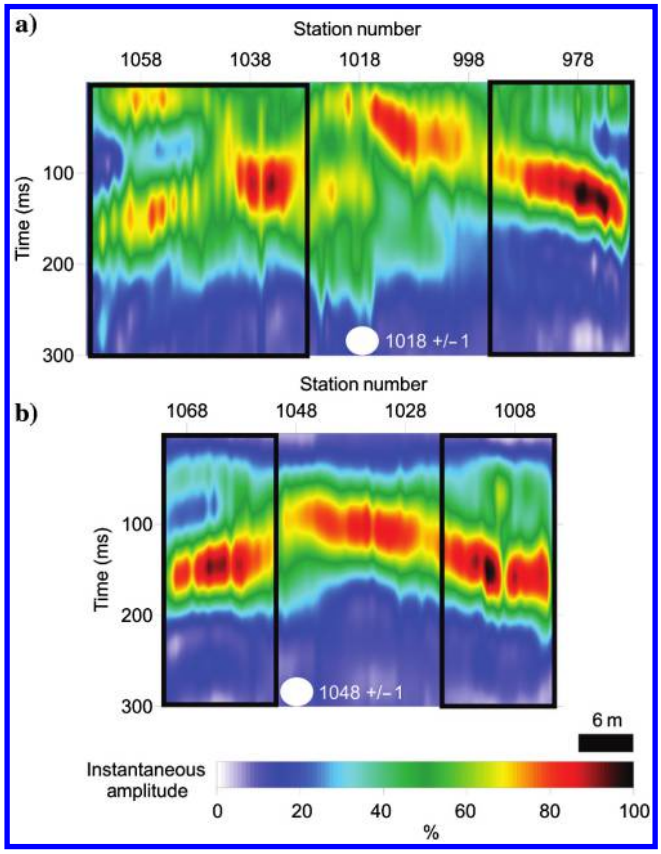

Figure 12. Complex BASW images comparing two different velocity regimes and anomaly depths combining forward- and reverse-acquisition schemes. (a) The test tunnel at 3 m deep and (b) the clandestine tunnel at 22 m deep. White circles and text denote both tunnel locations. Note the strikingly similar signatures for both images (black boxes).

tunnel. Although not advised, running the gamut from fundamental Rayleigh wave to P-wave correction velocities essentially allows faster earlier time events to sum into the receiver stack integrating the full-seismic wavefield. Initial studies show that overestimating the velocity correction may exaggerate the vertical separation of the anomaly signature, aiding its identification.

Quantitative amplitude analysis must consider the multimode nature of the forward-propagating surface wave and the scattered wavefield. Mode separation is critical to correctly delineate the various coherent signals emanating from lateral discontinuities. Estimation of the attenuation field in the presence of mode interference will lead to biased, contaminated results. Although they may provide supplementary information, measurements may be more related to mode excitation and interference patterns, rather than mode-specific anomaly responses. Careful filter design, specifically phase-velocity width and tapering, must seek a balance between one mode's removal and another's continuity. With closely spaced phase-velocity relationships, mode-superposition dispersion characteristics may negate filtering altogether. Conversely, in the absence of a dispersive regime, or HM generation, these categorical characterizations are unnecessary.

At its basic interpretation, our methods are imaging velocity variation across a site. The anomalies that are present in the complex BASW images represent deviations from the background velocity. If these changes were related to large-scale fluctuations, rather than local heterogeneities, it would be improbable for them to manifest consistently and symmetrically over purpose-built tunnels. A survey-wide velocity variation should also be found during the preliminary velocity-characterization phase of each analysis. Similarly, if part of a global trend, the various horizons of the image should fluctuate together. If we reevaluate Figure 13a, we have the linearly consistent background velocity trend along time zero and the anomalous tunnel signature that deviates from that relatively flat horizon. Moving to the higher velocity correction and filtered image, we can interpret a relatively smoothly varying velocity-structure change in Figure 13c. There, the horizon varies smoothly from approximately 50 to 75 ms from left to right. That is in stark contrast to the tunnel anomaly that varies from approximately 100 ms to greater than 200 ms across the survey line (Figure 13b).

Near-surface applications, such as seismic hazard analysis or engineering site characterization, often focus on the upper 30 m of a site (e.g., V_S 30). With highly energetic sources, and relatively longer SOs and/or geophone separation, we may increase the depth of investigation. This is necessary for areas where survey requirements extend much deeper from tens to hundreds of meters. Anomaly shape and size is much more variable. Common tunnels average 1m × 1m. Dissolution cavities may be smaller than this or orders of magnitude larger. Fault studies reveal extremely sharp lateral discontinuities and also usually deal with much larger cross-sectional areas in the order of tens to hundreds of meters square. Having focused on smaller anomalies, we are optimistic that these procedures may also be applied to larger scale studies.

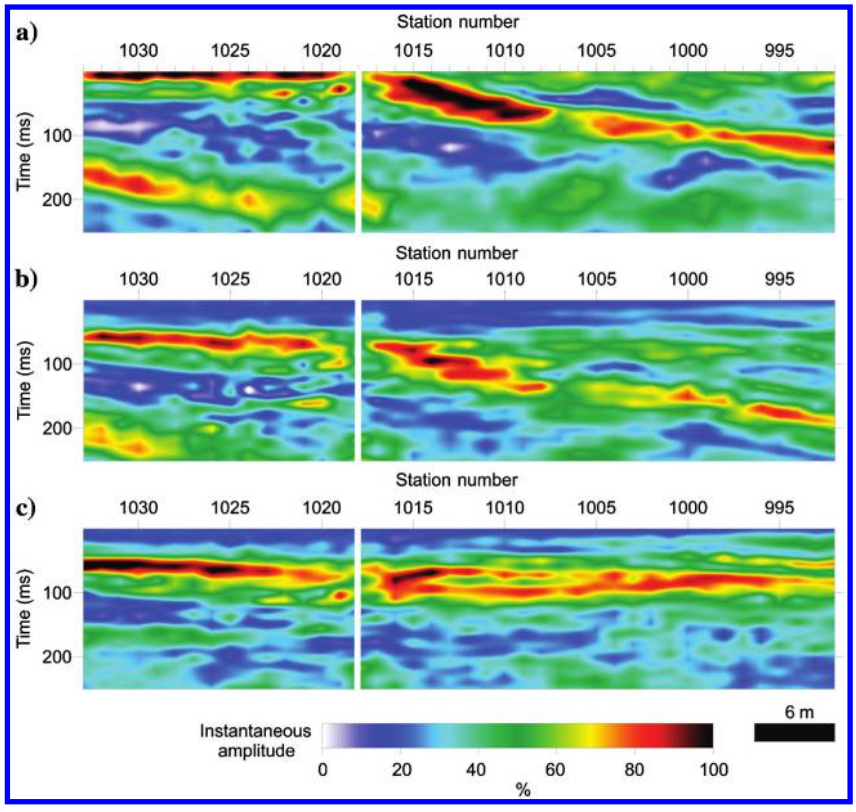

Figure 13. Correction-velocity comparison and wavefield separation with complex BASW analysis of the 3 m deep test tunnel with a 21.9 m SO and a unidirectional roll. From top to bottom: (a) fundamental correction velocity with full-wavefield standard analysis comparable with Figure 12a, (b) HM correction with full wavefield, and (c) HM correction with fundamental mute. A fundamental mute destroys the high-amplitude tunnel signature, as previously discussed with the other BASW techniques.

CONCLUSIONS

Our investigations highlight SWMs in the detection of anomalies with emphasis on tunnels. Most avenues of research were adapted from the classic BASW method. The use of multimode FV-LMOs in combination with surgical f-k muting for mode separation is seen as a major innovation of this study. In addition, the sampling shown here indicates correlation of BASW images enhances the localization of a void in unconsolidated media. Complex BASW and the 3D amplitude cube added attribute analysis to further differentiate the seismic wavefield and offer alternative imaging methods.

Correlation acts as a complementary attribute to the BASW image versus a stand-alone product. With this approach, we begin to move toward a quantitative, objective measurement versus a visual inspection. Future correlation research should resolve the current method's lack of robustness with outlier susceptibility and regularization. Moving beyond the current limitations of band-limited FV-LMO approximations, spectral decomposition methods could further define frequency-specific effects that are relatable to the depth of an anomaly. Moreover, nonlinear correlation of the time variables may be more appropriate given the sinusoidal nature of seismic waves. Finally, a more constrained or quantifiable justification for bin width is also proposed

as the current procedure balances resolution and smoothness in a purely subjective manner.

Complex BASW uses the sensitivity of the instantaneous-amplitude attribute to enhance the BASW technique. This treatment increases the robustness of the classic method by eliminating the need for f-k filtering of the forward-propagating wavefield and reducing the dependency of the analysis on velocity-correction accuracy. An avenue for future study is the coherence, slope, and amplitude variation along horizons of interest in the complex BASW images. At present, the method seems most responsive to the interference, and deflection, of the forward-propagating wavefield impinging on a subsurface anomaly. We hypothesize the complex attribute's success may be manifested in the conversion of phase to group characteristics. Further research is needed to judge the value of using the group properties of surface waves for anomaly detection.

In their present state, our SWMs have performed well and show promise in discovering near-surface anomalies. Our techniques reliably located tunnel voids at depths from 3 to 22 m. The BASW method lends itself to diversification, including the new advancements:

1) multimode BASW imaging and mode separation
2) BASW correlation analysis
3) instantaneous-amplitude integration
4) amplitude-cube visualization
5) complex BASW.

This expansion of the classic method provides an important leap forward for our investigations. We believe a multifaceted surface-wave evaluation would be a valuable addition to any anomaly-detection suite for geohazard assessment, security operations, and geologic characterization.

ACKNOWLEDGMENTS

Initial modeling was done at the University of Kansas, during the master's study of J. T. Schwenk. Many thanks go to the crew of the Exploration Services division of KGS for data acquisition within the United States. We also appreciate the efforts of deployed personnel for their collection of data outside the continental United States. Finally, we thank M. Brohammer for her thoughtful review of the manuscript.

REFERENCES

Anderson, N., T. Thitimakorn, A. Ismail, and D. Hoffman, 2007, A comparison of four geophysical methods for determining the shear wave velocity of soils: Environmental and Engineering Geoscience, **13**, 11–23, doi: 10.2113/gseegeosci.13.1.11.

Belfer, I., I. Bruner, S. Keydar, A. Kravtsov, and E. Landa, 1998, Detection of shallow objects using refracted and diffracted seismic waves: Journal of Applied Geophysics, **38**, 155–168, doi: 10.1016/S0926-9851(97)00025-6.

Bergamo, P., D. Boiero, and L. V. Socco, 2012, Retrieving 2D structures from surface-wave data by means of space-varying spatial windowing: Geophysics, **77**, no. 4, EN39–EN51, doi: 10.1190/geo2012-0031.1.

Bergamo, P., and L. V. Socco, 2014, Detection of sharp lateral discontinuities through the analysis of surface-wave propagation: Geophysics, **79**, no. 4, EN77–EN90, doi: 10.1190/geo2013-0314.1.

Boiero, D., and L. V. Socco, 2011, The meaning of surface wave dispersion curves in weakly laterally varying structures: Near Surface Geophysics, **9**, 561–570, doi: 10.3997/1873-0604.2011042.

Cardarelli, E., M. Cercato, A. Cerreto, and G. Di Filippo, 2010, Electrical resistivity and seismic refraction tomography to detect buried cavities: Geophysical Prospecting, **58**, 685–695, doi: 10.1111/gpr.2010.58.issue-4.

Davies, W. E., 1951, Mechanics of cavern breakdown: National Speleological Society, **13**, 6–43.

Dillon, L., and I. Lovett, 2013, Tunnel for smuggling found under border; tons of drugs seized: New York Times, 1 November, A14.

Dubrule, O., 2003, Geostatistics for seismic data integration in earth models: SEG and EAGE, SEG Distinguished Instructor Series 6.

Ernst, F. E., G. C. Herman, and A. Ditzel, 2002, Removal of scattered guided waves from seismic data: Geophysics, **67**, 1240–1248, doi: 10.1190/1.1500386.

Halliday, D., P. Bilsby, L. West, E. Kragh, and J. Quigley, 2015, Scattered ground-roll attenuation using model-driven interferometry: Geophysical Prospecting, **63**, 116–132, doi: 10.1111/gpr.2015.63.issue-1.

Hayashi, K., and H. Suzuki, 2004, CMP cross-correlation analysis of multichannel surface-wave data: Exploration Geophysics, **35**, 7–13, doi: 10.1071/EG04007.

Herman, G. C., P. A. Milligan, R. J. Huggins, and J. W. Rector, 2000, Imaging shallow objects and heterogeneities with scattered guided waves: Geophysics, **65**, 247–252, doi: 10.1190/1.1444715.

Ivanov, J., B. Leitner, W. Shefchik, J. T. Schwenk, and S. Peterie, 2013, Evaluating hazards at salt cavern sites using multichannel analysis of surface waves: The Leading Edge, **32**, 298–305, doi: 10.1190/tle32030298.1.

Ivanov, J., R. Miller, and G. Tsoflias, 2008, Some practical aspects of MASW analysis and processing: Symposium on the Application of Geophysics to Engineering and Environmental Problems, 1186–1198.

James, P., and P. Ferreira, 2013, Geophysical modeling of typical cavity shapes to calculate detection probability and inform survey design: Journal of Environmental and Engineering Geophysics, **18**, 297–316, doi: 10.2113/JEEG18.4.297.

Luo, Y., J. Xia, R. D. Miller, Y. Xu, J. Liu, and Q. Liu, 2008, Rayleigh-wave dispersive energy imaging using a high-resolution linear Radon transform: Pure and Applied Geophysics, **165**, 903–922, doi: 10.1007/s00024-008-0338-4.

Miller, R. D., J. Xia, C. B. Park, and J. M. Ivanov, 1999, Multichannel analysis of surfaces waves to map bedrock: The Leading Edge, **18**, 1392–1396, doi: 10.1190/1.1438226.

Park, C. B., R. D. Miller, and J. Ivanov, 2002, Filtering surface waves: Symposium for the Application of Geophysics to Engineering and Environmental Problems, SEI9.

Park, C. B., R. D. Miller, and J. Xia, 1998, Ground roll as a tool to image near-surface anomaly: 68th Annual International Meeting, SEG, Expanded Abstracts, 874–877.

Pearson, K., 1895, Contribution to the mathematical theory of evolution. Part II: Skew variation in homogeneous material: Philosophical Transactions of the Royal Society of London, Series A, **186**, 343–414, doi: 10.1098/rsta.1895.0010.

Peterie, S. L., and R. D. Miller, 2015, Near-surface scattering phenomena and implications for tunnel detection: Interpretation, **3**, no. 1, SF43–SF54, doi: 10.1190/INT-2014-0088.1.

Samyn, K., A. Bitri, and G. Grandjean, 2013, Imaging a near-surface feature using cross-correlation analysis of multi-channel surface wave data: Near Surface Geophysics, **11**, 1–10, doi: 10.3997/1873-0604.2012007.

Santos, F., 2014, Border's new sentinels are robots, penetrating deepest drug routes: New York Times, 23 February, A16.

Schwartz, A., 1974, Calculus and analytic geometry, 3rd ed.: Holt, Rinehart, and Winston.

Schwenk, J. T., R. Miller, J. Ivanov, S. Sloan, and J. McKenna, 2012a, Dispersion interpretation from synthetic seismograms and multi-channel analysis of surface waves (MASW): 82nd Annual International Meeting, SEG, Expanded Abstracts, doi: 10.1190/segam2012-1534.1.

Schwenk, J. T., R. Miller, J. Ivanov, S. Sloan, and J. McKenna, 2012b, Joint analysis of MASW and refraction traveltime tomography: Symposium for the Application of Geophysics to Engineering and Environmental Problems, 197–206, doi: 10.4133/1.4721744.

Shah, T., and A. J. Rubin, 2011, Taliban breach Afghan prison: Hundreds free: New York Times, 26 April, A1.

Sloan, S. D., S. L. Peterie, J. Ivanov, R. D. Miller, and J. R. McKenna, 2010, Void detection using near-surface seismic methods, *in* R. D. Miller, J. D. Bradford, and K. Holliger, eds., Advances in near-surface seismology and ground-penetrating radar: SEG Geophysical Developments Series 15, 201–218.

Sloan, S. D., S. L. Peterie, R. D. Miller, J. Ivanov, J. T. Schwenk, and J. R. McKenna, 2015, Detecting clandestine tunnels using near surface seismic techniques: Geophysics, **80**, no. 5, EN127–EN135, doi: 10.1190/geo2014-0529.1.

Sloan, S. D., S. L. Peterie, R. D. Miller, T. L. Snow, J. R. McKenna, and O. M. Metheny, 2013, In-theater seismic acquisition: Operational examples from a tunnel detection team: 83rd Annual International Meeting, SEG, Expanded Abstracts, 1801–1805.

Socco, L. V., D. Boiero, S. Foti, and R. Wisén, 2009, Laterally constrained inversion of ground roll from seismic reflection records: Geophysics, **74**, no. 6, G35–G45, doi: 10.1190/1.3223636.

Socco, L. V., S. Foti, and D. Boiero, 2010, Surface-wave analysis for building near-surface velocity models — Established approaches and new perspectives: Geophysics, **75**, no. 5, 75A83–75A102, doi: 10.1190/1.3479491.

Strobbia, C., A. Zarkhidze, F. Ibrahim, and R. May, 2014, Model-based attenuation for scattered dispersive waves: Geophysical Prospecting, **62**, 1143–1161, doi: 10.1111/gpr.2014.62.issue-5.

Taner, M. T., F. Koehler, and R. E. Sheriff, 1979, Complex seismic trace analysis: Geophysics, **44**, 1041–1063, doi: 10.1190/1.1440994.

Tokimatsu, K., S. Tamura, and H. Kojima, 1992, Effects of multiple modes on Rayleigh wave dispersion characteristics: Journal of Geotechnical Engineering, American Society of Civil Engineering, **118**, 1529–1543, doi: 10.1061/(ASCE)0733-9410(1992)118:10(1529).

van der Veen, M., R. Spitzer, A. G. Green, and P. Wild, 2001, Design and application of a towed land-streamer system for cost-effective 2-D and pseudo-3-D shallow seismic data acquisition: Geophysics, **66**, 482–500, doi: 10.1190/1.1444939.

Vignoli, G., and G. Cassiani, 2009, Identification of lateral discontinuities via multi-offset phase analysis of surface wave data: Geophysical Prospecting, **58**, 389–413, doi: 10.1111/(ISSN)1365-2478.

Watabe, Y., and S. Sassa, 2008, Application of MASW technology to identification of tidal flat stratigraphy and its geoenvironmental interpretation: Marine Geology, **252**, 79–88, doi: 10.1016/j.margeo.2008.03.007.

Xia, J., R. D. Miller, and C. B. Park, 1999, Estimation of near-surface shear-wave velocity by inversion of Rayleigh waves: Geophysics, **64**, 691–700, doi: 10.1190/1.1444578.

Zeng, C., J. Xia, R. D. Miller, and G. P. Tsoflias, 2011, Application of the multiaxial perfectly matched layer (M-PML) to near-surface seismic modeling with Rayleigh wave: Geophysics, **76**, no. 3, T43–T52, doi: 10.1190/1.3560019.